

Article

Not peer-reviewed version

---

# Effect of Cooling Rate on Microstructure Evolution and Mechanical Properties of SCM435 Steel

---

[Jilin Chen](#)<sup>\*</sup>, Guanghong Feng, [Yaxu Zheng](#)<sup>\*</sup>, Yuming Zhang, [Peng Lin](#), Lijun Wang, Yongchao Li

Posted Date: 25 December 2023

doi: 10.20944/preprints202312.1857.v1

Keywords: SCM435; cold heading steel; cooling rate; oxidation; microstructure



Preprints.org is a free multidiscipline platform providing preprint service that is dedicated to making early versions of research outputs permanently available and citable. Preprints posted at Preprints.org appear in Web of Science, Crossref, Google Scholar, Scilit, Europe PMC.

Copyright: This is an open access article distributed under the Creative Commons Attribution License which permits unrestricted use, distribution, and reproduction in any medium, provided the original work is properly cited.

Disclaimer/Publisher's Note: The statements, opinions, and data contained in all publications are solely those of the individual author(s) and contributor(s) and not of MDPI and/or the editor(s). MDPI and/or the editor(s) disclaim responsibility for any injury to people or property resulting from any ideas, methods, instructions, or products referred to in the content.

Article

# Effect of Cooling Rate on Microstructure Evolution and Mechanical Properties of SCM435 Steel

Jilin Chen <sup>1,2,3, \*</sup>, Guanghong Feng <sup>1</sup>, Yaxu Zheng <sup>4,5,6, \*</sup>, Yuming Zhang <sup>2,3</sup>, Peng Lin <sup>7</sup>  
and Lijun Wang <sup>2,3</sup> and Yongchao Li <sup>2,3</sup>

<sup>1</sup> Metallurgical Technology Institute, Central Iron and Steel Research Institute, Beijing 100081, PR. China

<sup>2</sup> Hebei Xinggang Technology Co., LTD, Xingtai 054027, PR. China.

<sup>3</sup> Xing tai Iron and Steel Co., Ltd , Xingtai 054027, PR. China.

<sup>4</sup> School of Material Science and Engineering, Hebei University of Science and Technology, Shijiazhuang 050018, PR. China.

<sup>5</sup> Hebei Key Laboratory of Material Near-Net Forming Technology, Shijiazhuang 050018, PR. China.

<sup>6</sup> Hebei Engineering Laboratory of Aviation Lightweight Composite Materials and Processing Technology, Shijiazhuang 050018, PR. China.

<sup>7</sup> Hebei Institute of Mechanical and Electrical Technology, Xingtai 054000, PR. China

\* Correspondence: chenjl@xtsteel.com (J.C.); zhengyaxu1984@163.com (Y.Z.)

**Abstract:** The microstructure evolution of SCM435 cold heading steel at different cooling rates was investigated by means of scanning electron microscopy, TEM, XRD, and electron backscatter diffraction. The results show that the cooling rate has a significant effect on the microstructure of the experimental steel. With an acceleration of the cooling, the microstructure of the steel gradually changed from ferrite and pearlite to ferrite, pearlite, and granular bainite; finally, the pearlite disappeared, and the microstructure changed to acicular ferrite, bainite, and martensite. With an increase in the cooling rate, the morphology of the carbide underwent an evolution from sheet carbide to short-rod carbide, granular carbide, and ultimately thin-strip carbide. With the acceleration of cooling, the proportion of large-angle grain boundaries gradually decreased, and the area of small-angle grain boundaries gradually increased. When the cooling rate was 0.1°C/s, the proportion of large-angle grain boundaries was as high as 52.8%, and the dislocation density was only  $1.91 \times 10^{12} \text{ cm}^{-2}$ . When the cooling rate was 2.0°C/s, the proportion of large-angle grain boundaries was only 27.1%, and dislocation density increased to  $5.38 \times 10^{12} \text{ cm}^{-2}$ . With the increase in the cooling rate, the depth of the decarbonization layer and the thickness of the scale oxide gradually decreased, the proportion of FeO phase in the scale phase gradually decreased, and the proportion of Fe<sub>3</sub>O<sub>4</sub> phase and Fe<sub>2</sub>O<sub>3</sub> phase gradually increased. The tensile strength increased monotonously with the increase in cooling rate, whereas the elongation and shrinkage first decreased, then increased, and then decreased. When the cooling rate was 1.0 m/s, the short rod and granular bainite in the material structure endowed the SCM435 steel with excellent strength and toughness matching, and the tensile strength and elongation of the steel reached 895 MPa and 24%, respectively.

**Keywords:** SCM435; cold heading steel; cooling rate; oxidation; microstructure

## 1. Introduction

Cr–Mo microalloyed high-strength fasteners are being used more frequently, and they are commonly used as 10.9–12.9 high-strength bolts <sup>[1–4]</sup> through the complete solid solution of Cr and Mo in ferrite, improving its strength <sup>[5]</sup> without reducing its plasticity, and can inhibit the precipitation of carbide in the tempering process of steel. Thus, it is advantageous to use a tempering method as a heat treatment <sup>[6–8]</sup>. In our test steel, chromium is mainly used to improve its strength and to maintain its toughness after tempering. Moreover, molybdenum (Mo) improves the hardenability and thermal strength of steel to prevent tempering brittleness. Mo can make parts with large sections deeper and quenched. Mo improves the tempering resistance or tempering stability of steel so that parts can be tempered at higher temperatures to eliminate (or reduce) residual stress and effectively improve plasticity <sup>[9–11]</sup>.

The goal of controlled rolling and controlled cooling technology for high-strength cold heading steel is to obtain a material microstructure and mechanical properties that meet the various needs of deep processing [12-14]. In particular, the cooling rate of high-strength cold heading steel determines its physical quality: the material phase composition, grain orientation, dislocation distribution, and physical properties [15-16]. Therefore, our study of the effect of the cooling rate on the laws of structure evolution aims to propose a high-quality, strong-plastic-matching control process for cooling, reveal the regulation law for the microstructural properties of high-strength cold heading steel during cooling, build a theoretical system for the strength and toughness of high-strength cold heading steel, and establish a combined mechanism model for strength and toughness.

In the process of controlling rolling and controlled cooling to ensure the toughness of materials, the decarburization and oxidation state of steel are often overlooked. Firstly, the decarburization and oxidation behavior of steel are inevitable during the heating and cooling processes, and they are influenced by multiple factors such as composition, temperature, and cooling rate, making it extremely complex [17-19]. However, there are rare reports on considering the influence of cooling rate on surface decarburization and oxidation behavior in theory, both domestically and internationally [20,21]. Therefore, achieving a balance between the internal structure toughness of high-strength cold heading steel and the surface decarburization and oxidation matching is the main research objective of this paper.

## 2. Materials and Methods

The chemical composition of SCM435 is shown in Tab. 1. Its smelting process was as follows: 80t converter smelting, ladle furnace refining, Ruhrstahl Hausen vacuum degassing, and continuous casting under dynamic light reduction to  $280 \times 325$  mm. The rectangular billet became a square billet of size  $160 \times 160$  mm after nine bloom passes. This process was carried out on the industrial production line of a high-speed wire rod mill.

**Table 1.** Chemical composition of SCM435 microalloyed steels (wt%).

Steel	C	Si	Mn	P	S	Cr	Mo
SCM435	0.35	0.18	0.82	0.001	0.0008	0.98	0.22

In the industrial production line of a high-speed wire rolling mill, a square billet of  $160 \text{ mm} \times 160 \text{ mm}$  was heated in a regenerative heating furnace at  $1100^\circ\text{C}$  and then held for 120 min after six rough rolling, eight medium rolling, four prefinishing, eight finishing, and four reduced diameter rolling passes. After spinning, a Stelmor cooling line (length = 110 m) was slowly cooled. The design of the rolling process is shown in Table 2.

**Table 2.** Rolling technology for SCM435 steels.

Process	Heating temperature/ $^\circ\text{C}$	Finishing temperature/ $^\circ\text{C}$	Heat cover	Blower	Cooling rate / m/s
1	$1100 \pm 10$	$900 \pm 10$	Close	Close	0.1
2	$1100 \pm 10$	$900 \pm 10$	Open	Close	0.5
3	$1100 \pm 10$	$900 \pm 10$	Open	Open	1.0
4	$1100 \pm 10$	$900 \pm 10$	Open	Open	1.5
5	$1100 \pm 10$	$900 \pm 10$	Open	Open	2.0

The sample was cut from a hot rolled wire rod. After the metallographic sample was ground and polished in the vertical direction, the sample was etched for 10 s with 4%  $\text{HNO}_3$ +96%  $\text{C}_2\text{H}_5\text{OH}$  (volume fraction, the same below) solution, and then the tissue was observed through a JSM-5610LV scanning electron microscope. The fine structure was observed through a JEM-2010 transmission electron microscope. XRD was used to detect the diffraction peak. A classical empirical formula was used to calculate the diffraction parameters, where the scanning area was set to  $15 \times 10$  mm, the scanning voltage was set to 40 kV, the current was set to 40 mA, the X-ray diffraction step was set to

0.02°, and the range of the scanning angle for the diffraction peak was 20° (2 $\theta$ )–120° (2 $\theta$ ). The electron backscatter diffraction (EBSD) system module (Oxford symmetry) installed in the Zeiss Gemini scanning electron microscope was used to measure the effective grain size, crystallographic orientation, grain boundary distribution, and phase structure of the oxide in the experimental steel under different conditions. We used an EBSD scan step of 0.1  $\mu\text{m}$ . According to the requirements of GB/T228, a tensile sample was intercepted along the rolling direction, and tensile testing was carried out using a WAW500 universal tensile testing machine at room temperature.

### 3. Experimental Results and Discussion

#### 3.1. Microstructure

The microstructure of the experimental steel at different cooling speeds was observed with the use of scanning electron microscopy (SEM), as shown in Figure 1. The experimental results show that with an increase in the cooling rate, the microstructure gradually changes from ferrite (F)+pearlite (P) to F+P+granular bainite (GB), and then the pearlite disappears, and finally the microstructure changes to F+bainite (B)+martensite (M). When the cooling rate is 0.1°C/s, the microstructure of the experimental steel is an irregular polygonal ferrite and lamellar pearlite. Under SEM, the grey-black phase group is divided into ferrite, and the bright white phase group is divided into pearlite, in which the proportion of ferrite is 61%, as shown in Figure 1(a). When the cooling rate is 0.5°C/s, the amount of ferrite in the experimental steel is significantly reduced, some pearlite in the structure is distributed in granular form along the ferritic grain boundary, and GB begins to precipitate in the microstructure, as shown in Figure 1(b). With a further increase in the cooling rate, acicular ferrite (AF) forms in the microstructure, and the pre-eutectoid ferrite coexists with random massive ferrite. When the cooling rate is 1.5°C/s, the pearlite phase in the material matrix disappears, the proportion of the bainite phase further increases to 78%, and the bainite exists in two forms: one form has an irregularly intersecting short-rod or granular distribution, with granular cementite distributed in short-rod-like bainite, and the other is lamellar bainite with a certain orientation. The AF phase accounts for only 5%, as shown in Figure 1(d). When the cooling rate reaches 2°C/s, the proportion of the bainite phase in the matrix is reduced to 63%, and martensite precipitation appears, as shown in Figure 1(e). According to this analysis, when the cooling speed is 0.1–1.5°C/s, the austenite transforms to ferrite (A→F); when the cooling speed is 0.1–1.0°C/s, the pearlite transformation (A→P); when the cooling speed is 0.5–2.0°C/s, the bainite transformation (A→B); and when the cooling speed is 2.0°C/s, the martensite transformation (A→M).

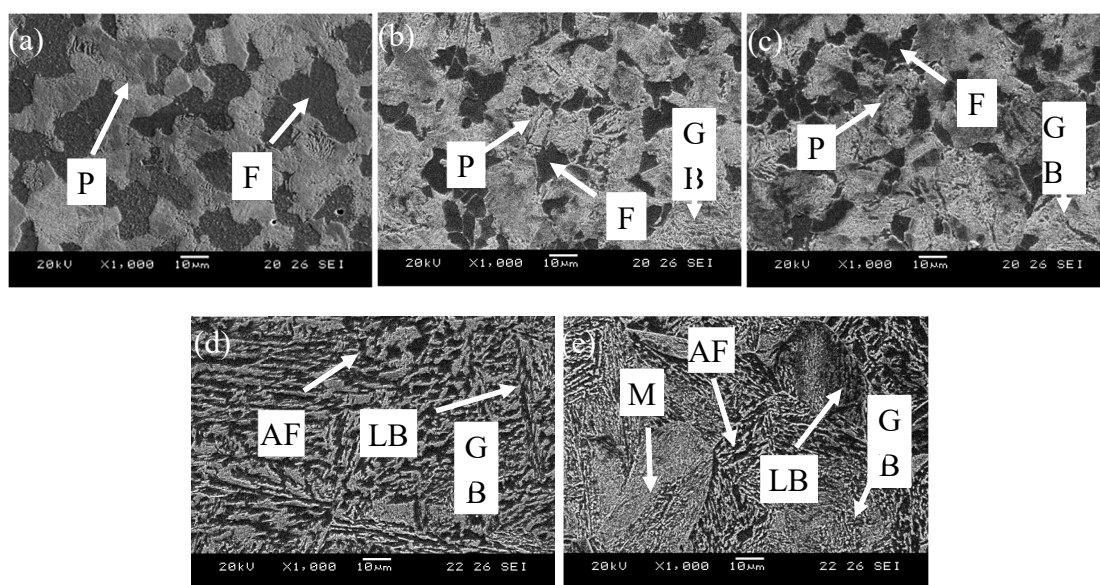


**Figure 1.** Microstructure evolution of steel under different cooling rates: (a) 0.1°C/s; (b) 0.5°C/s; (c) 1°C/s; (d) 1.5°C/s; (e) 2°C/s.

### 3.2. Carbide morphology

Figure 2 shows TEM images of the carbide morphology in the microstructure of the experimental steel for different cooling rates. It can be seen that the carbide morphology of high-strength cold heading steel forms quite differently at different speeds of cooling: with an increase in cooling speed, the carbide morphology obeys the law of evolution for sheet carbide, short-rod carbide, granular carbide, and thin-strip carbide. It is evident from the analysis that when the cooling rate is  $0.1^{\circ}\text{C/s}$ , carbides have a certain distribution in a transverse orientation to the austenite. The flake carbide group is separated by the austenite grain boundary, and it has distinct orientation rules. The flake carbide is a carbon-rich zone of the matrix. The distance between them determines the strength and plasticity of a material. As shown in Figure 2(a), when the cooling rate is  $0.5^{\circ}\text{C/s}$ , some of the continuous lamellar carbides are interrupted to form short rod-like carbides, as shown in Figure 2(b), which means that at a certain degree of supercooling, the austenite grains form unevenly dispersed cementates. At the phase transition, short rod-like carbides are immediately formed. At this time, the carbides maintain a certain orientation relationship. When the cooling rate is  $1.0^{\circ}\text{C/s}$ , the short rod-like carbides are fine and further dispersed, which shows that most of the granular carbides with fixed orientations are dispersed and distributed in the ferrite phase. However, some carbides begin to disperse and grow around the original orientation to form a kind of granular island, as shown in Figure 2(c). In this state, the material has better plasticity. When the cooling rate is  $1.5^{\circ}\text{C/s}$ , the granular carbide particles in the ferrite phase grow larger, and thin strips of carbides appear in the matrix. The formation temperature of the carbides is approximately  $400^{\circ}\text{C}$ . As the cooling rate increases to  $2.0^{\circ}\text{C/s}$ , the coniferous thin strips of carbide become darker and finer in shape, as shown in Figure 2(e). Local lath martensite can be observed.

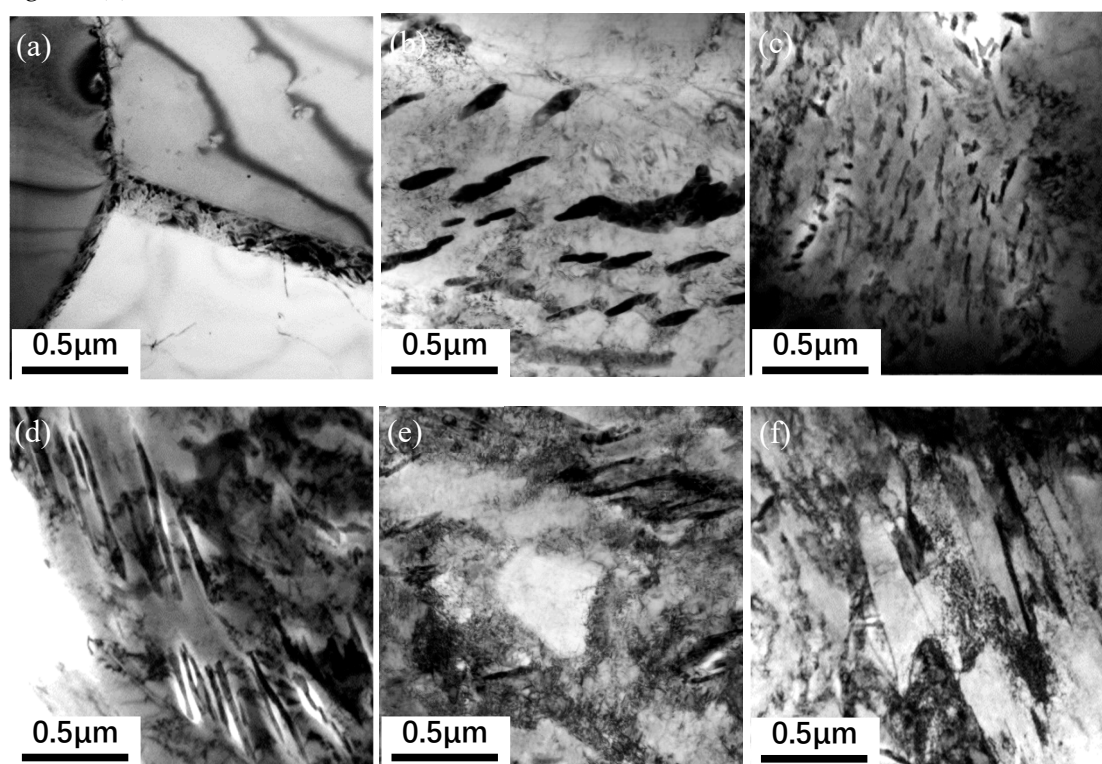
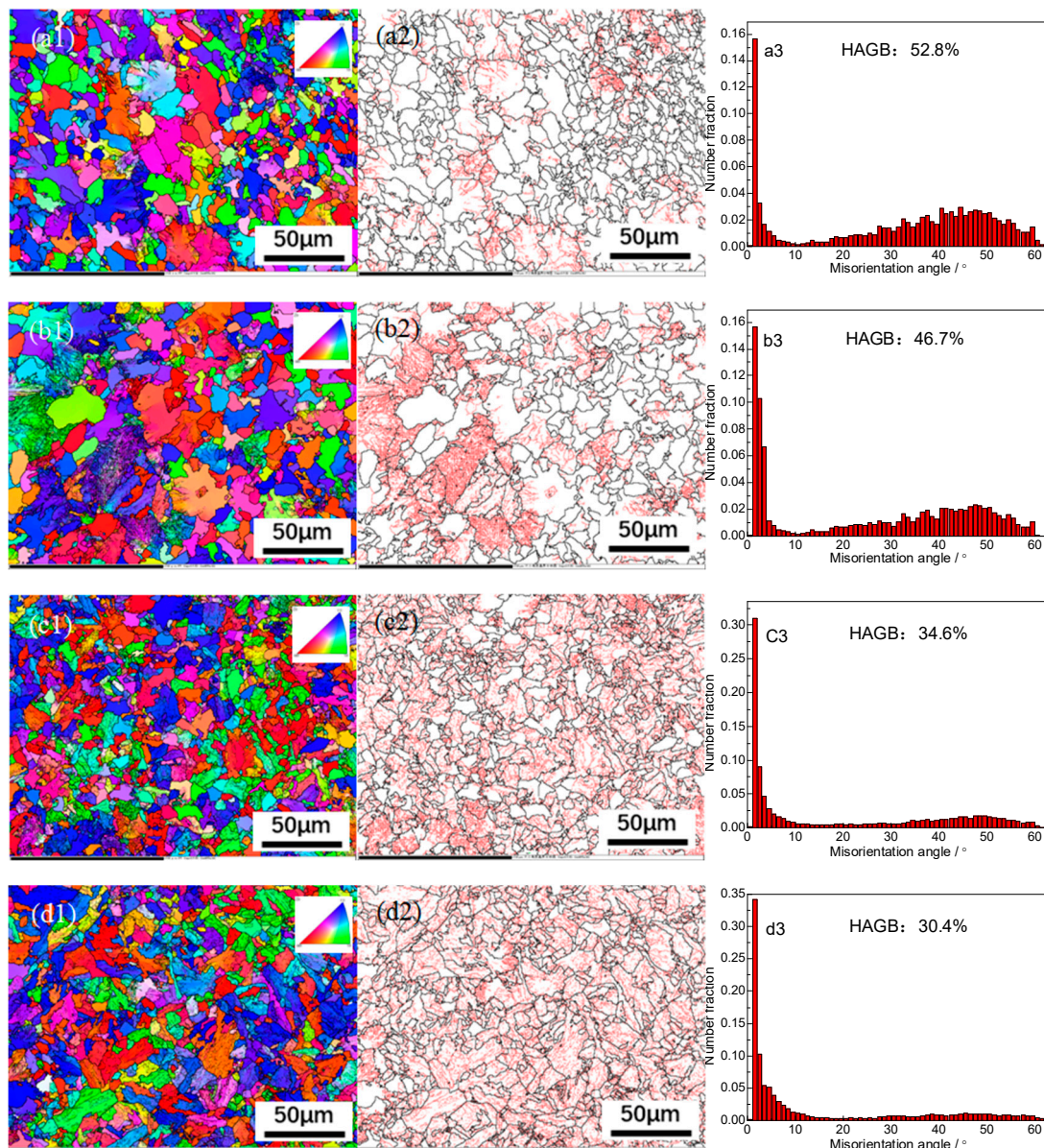


**Figure 2.** Carbide morphology under different cooling rates of steel. (a)  $0.1^{\circ}\text{C/s}$ : Flake carbide; (b)  $0.5^{\circ}\text{C/s}$ : short-rod carbide; (c)  $1^{\circ}\text{C/s}$ : granular carbide; (d)  $1.5^{\circ}\text{C/s}$ : thin-strip carbide; (e)  $2^{\circ}\text{C/s}$  sliver carbide; (f)  $2^{\circ}\text{C/s}$ : lath martensite.

### 3.3. Grain boundary orientation

EBSD technology was used to characterize the grain boundary orientation characteristics of high-strength cold heading steel cooled at different cooling rates, as shown in Figure 3. Figure 3(a1)–(e1) shows the orientation images at the cooling rates of  $0.1^{\circ}\text{C/s}$ ,  $0.5^{\circ}\text{C/s}$ ,  $1.0^{\circ}\text{C/s}$ ,  $1.5^{\circ}\text{C/s}$ , and  $2.0^{\circ}\text{C/s}$ ,

respectively. Figure 3(a2)–(e2) shows the distribution diagrams of the grain boundaries of the experimental steel cooled at different cooling rates, which represent the distribution of the grain boundary size and angle in the visual field matrix, and the detection results can be seen. With an acceleration of cooling, the proportion of large-angle grain boundaries (having an orientation difference of  $>15^\circ$ ) gradually decreases, and the distribution area of small-angle grain boundaries (orientation difference  $<15^\circ$ ) in the red region gradually increases, which means that the proportion of small-angle grain boundaries is gradually increasing. Figure 3(a3)–(e3) shows the distribution of orientation differences at the corresponding cooling rate and characterizes the proportion of large- and small-angle grain boundaries. When the cooling rate is  $0.1^\circ\text{C/s}$ , the proportion of large-angle grain boundaries is the highest at 52.8%; when the cooling rate is  $2.0^\circ\text{C/s}$ , the proportion of large-angle grain boundaries is the lowest at only 27.1%. With an acceleration in cooling, the dislocation density continues to increase, the disordered entanglement dislocation in the ferritic crystals gradually transitions from an orderly distribution to an irregular arrangement, and the dislocations sharpen to form small-angle grain boundaries (orientation difference  $<15^\circ$ ). Large-angle grain boundaries can hinder crack initiation and propagation during impact fracture and improve the impact energy of high-strength cold heading steel, which then improves the toughness of the material.



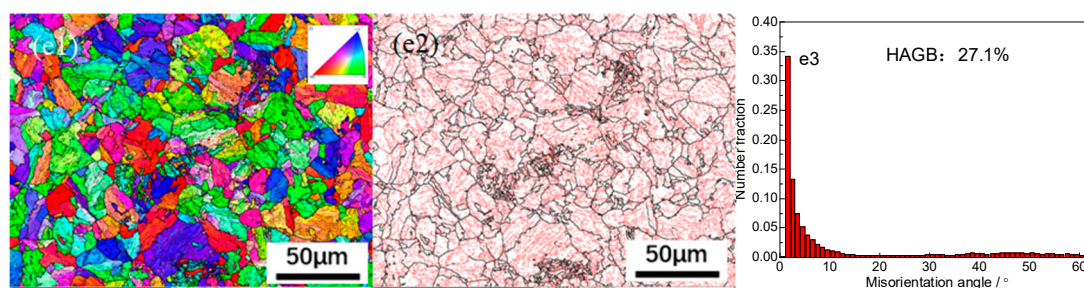


**Figure 3.** EBSD analysis results for different cooling rates of steel. Grain orientation imaging: (a1, b1, c1, d1, e1); grain boundary distribution map of large and small angles: (a2, b2, c2, d2, e2); grain boundary misorientation distribution map: (a3, b3, c3, d3, e3); 0.1°C/s (a1, a2, a3); 0.5°C/s (b1, b2, b3); 1°C/s (c1, c2, c3); 1.5°C/s (d1, d2, d3); 2°C/s (e1, e2, e3).

The experimental results show that from 0.1°C/s to 2.0°C/s, the proportion of large-angle grain boundaries in the experimental steel decreases by 25.7%. It can be seen that the effect of the cooling rate on the large-angle grain boundaries is between the effect of the final rolling temperature and spinning temperature on grain orientation, which indicates that the final rolling temperature is a deformation parameter. The influence of the dynamic recovery mechanism and recrystallization is greater than that of the cooling rate, and the influence of the cooling rate mechanism is greater than that of static recovery or the initial cooling temperature of recrystallization. The effective grain size of the experimental steel increases significantly with an increase in the cooling rate, which is mainly affected by the cooling degree and the microstructure transformation.

### 3.4. Dislocation density

The distribution of dislocations at different cooling rates was characterized and analyzed. The evolution of the dislocation morphology was observed under TEM, as is shown in Figure 4. At various cooling speeds, dislocations occur in the microstructure, which takes the form of bundles of roughly parallel massive ferrite and a nonlayered structure composed of intermingled cementite. However, our comparison shows that the dislocation density in the fine structure of the material is significantly higher for high-speed cooling than for low-speed cooling, as shown in Fig. 4. Cooling rates below 1.0°C/s result in improved dislocation density.

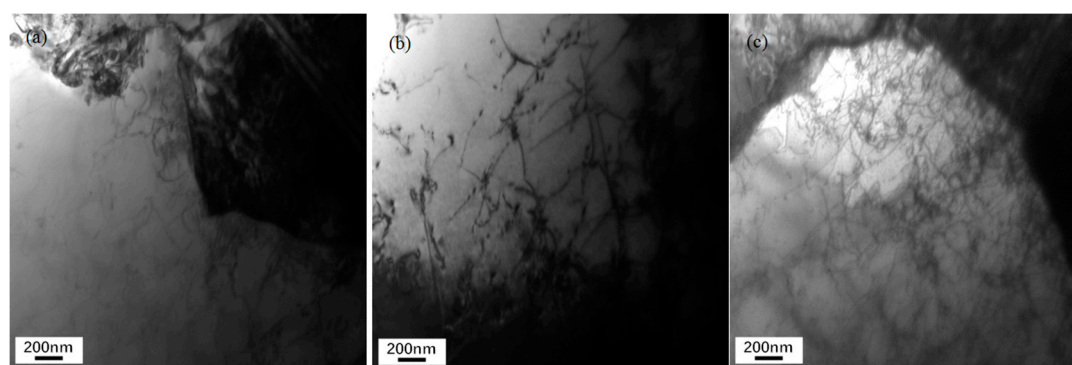


**Figure 4.** Dislocations in steel under different cooling rates: (a) 0.1°C/s; (b) 1°C/s; (c) 2°C/s.

XRD was used to measure the diffraction pattern of the experimental steel under different cooling rates and temperatures, and the density of dislocations in the steel was calculated using the modified Williamson–Hall formula (MWH), as shown in Table 3. According to the calculated value of dislocation density, the corresponding microstructure evolution analysis shows that the experimental steel is only  $2.18 \times 10^{12} \text{ cm}^{-2}$  at a cooling rate of 0.5°C/s, and the dislocation density of the experimental steel increases exponentially at 2.0°C/s. In combination with the microstructure evolution, a large proportion of the grain boundaries in the experimental steel microstructure are

small-angle grain boundaries, which further verifies the close relationship between the proportion of small-angle grain boundaries and the measure of dislocation density and also verifies the corresponding relationship between dislocation entanglement and small-angle grain boundaries in the bainite and martensite microstructure.

**Table 3.** Measured value of dislocation density of experimental steel.

Steel	Dislocation density / $10^{12} \bullet \text{cm}^{-2}$				
	0.1°C/s	0.5°C/s	1.0°C/s	1.5°C/s	2.0°C/s
	1.91	2.18	2.98	4.19	5.38

### 3.5. Phase structure of oxide

The EBSD analysis results for the distribution of scale phase on the surface of the experimental steel for different cooling rates are shown in Figure 5. The test results show that with the acceleration of the cooling rate, the thickness of the oxide sheet on the surface of the material gradually decreases, which is consistent with our observation using the microscope. The phase structure is mainly FeO phase, Fe<sub>3</sub>O<sub>4</sub> phase, and a small amount of Fe<sub>2</sub>O<sub>3</sub> phase, and the interphase gap is large. With an acceleration of cooling, the proportion of FeO phase gradually decreases, and the proportion of Fe<sub>3</sub>O<sub>4</sub> and Fe<sub>2</sub>O<sub>3</sub> phases increases gradually. It can be seen from the test data that in the cooling speed range of 0.1–0.5°C/s, the oxide phase is dominated by FeO phase and Fe<sub>3</sub>O<sub>4</sub> phase, which account for 54% and 43%, respectively. The phase structure of the oxide layer has no obvious stratification and is in a cross-mixed distribution state. When the cooling rate rises to 1.0°C/s, the proportion of FeO phase and Fe<sub>3</sub>O<sub>4</sub> phase becomes 31% and 58%, respectively. At this cooling rate, the FeO phase and Fe<sub>3</sub>O<sub>4</sub> phase are evenly distributed inside and outside, and the Fe<sub>2</sub>O<sub>3</sub> phase is scattered throughout the FeO phase and Fe<sub>3</sub>O<sub>4</sub> phase. When the cooling rate is 2.0°C/s, no oxide sheet is found under EBSD. The experiment shows that when the cooling rate is controlled in the range of 0.1–1.0°C/s, the transformation of the oxide sheet is mainly FeO phase, Fe<sub>3</sub>O<sub>4</sub> phase, and a small amount of Fe<sub>2</sub>O<sub>3</sub> phase. The acceleration of the cooling rate is conducive to an increase in the proportion of Fe<sub>3</sub>O<sub>4</sub> phase, and the corrosion protection of the surface oxide layer is maintained as the oxide sheet thins.

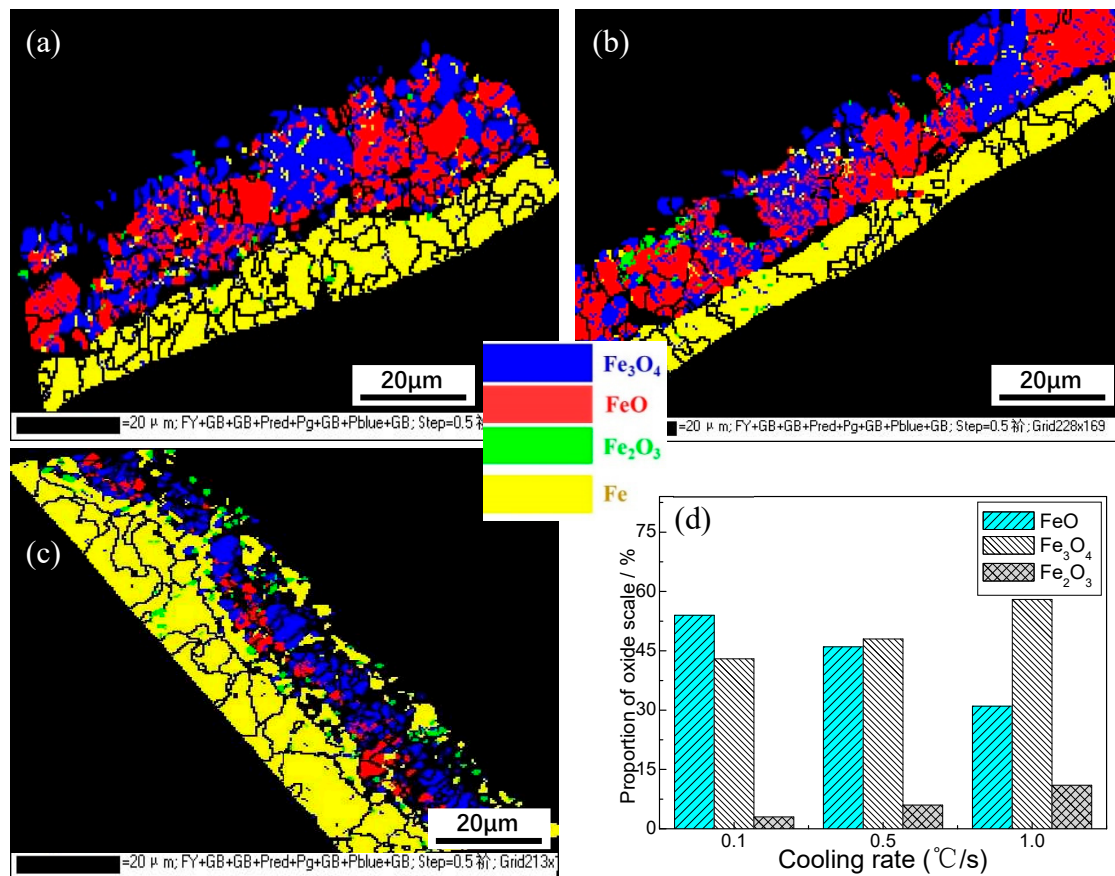


**Figure 5.** EBSD scale analysis of steel for different cooling rates: (a) 0.1°C/s; (b) 0.5°C/s; (c) 1.0°C/s; (d) phase distribution map.

### 3.6. Surface decarburization

Metallographic observations were taken of the surface decarburization structure of the experimental steel cooled at different cooling rates; the decarburization structure of the sample is shown in Figure 6. The results show that the surface decarburization of steel decreases gradually with an increase in the cooling rate, and the decarburization layer is inhibited when the cooling rate is higher than 1.5°C/s. When the cooling rate is 0.1°C/s, the fully decarburized layer and the partially decarburized layer coexist, as is shown in Figure 6a. When the cooling velocity reaches 1.0°C/s, a complete decarburization layer of 4 μm and a partial decarburization layer of 10 μm remain on the surface. When the cooling rate is greater than 1.5°C/s, no decarburization layer is detected. This experiment shows that the acceleration of the cooling rate inhibits the surface decarburization of steel. When the cooling rate is  $\geq 1.5$ °C/s, there is no decarburization on the surface of the steel. The inhibition by the cooling speed of the decarbonization transformation is mainly reflected in the reduction of the residence time of the steel in the high-temperature section. We estimate that at 0.1°C/s, it takes 25 min for the temperature to drop from 850°C to 700°C, which means that the decarbonization of the steel continues at 700–850°C. When the cooling speed is 1.0°C/s, it only takes 2.5 min for the temperature to drop below 700°C. The diffusion of carbon atoms is significantly inhibited.

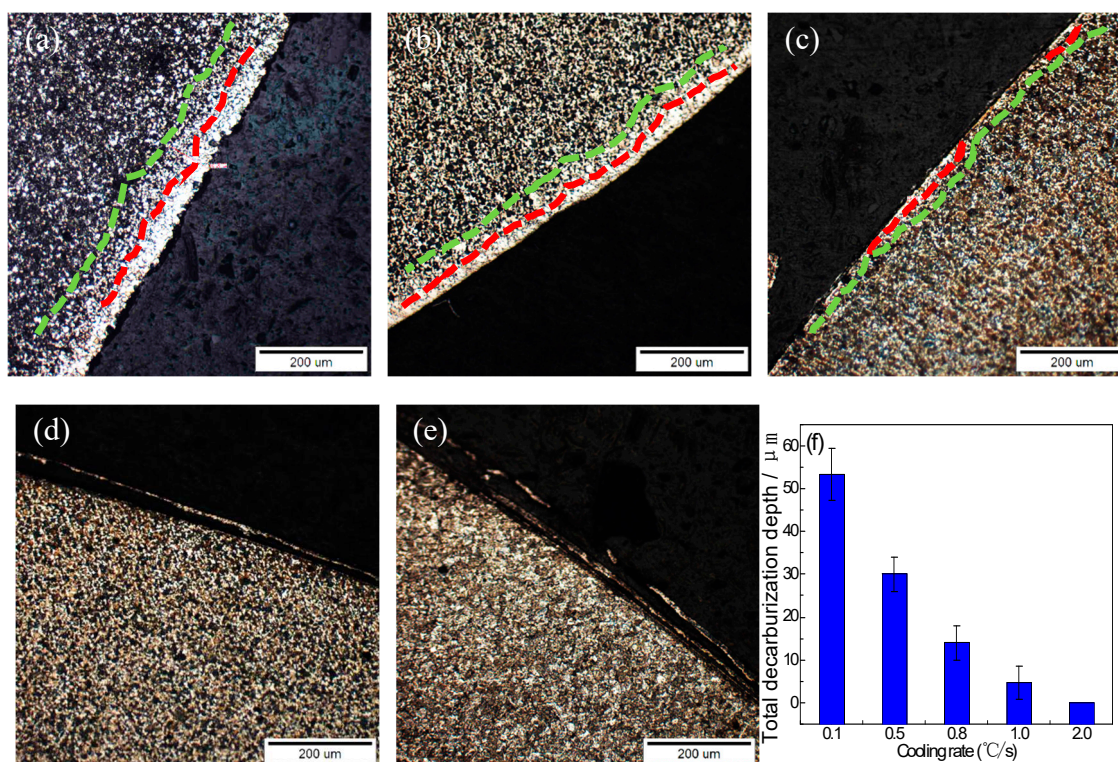


**Figure 6.** Decarburization layer morphology of steel for different cooling rates: (a) 0.1°C/s; (b) 0.5°C/s; (c) 1.0°C/s; (d) 1.5°C/s; (e) 2.0°C/s; (f) curve of decarburization depth.

### 3.7. Mechanical property

The tensile stress–strain curves of the SCM435 steel at room temperature for different cooling rates are shown in Figure 7. It can be seen that the SCM435 steel has no obvious yield platform at room temperature, and its resistance to microplastic deformation in the initial stage of the tensile experiment is not obvious. With an increase in the cooling rate, the tensile strength ( $\sigma_b$ ) gradually increases, and the elongation and shrinkage after fracture first decrease, then increase, and then decrease. When the cooling rate is 0.1 m/s, the tensile strength ( $\sigma_b$ ) of the material under slow cooling is 708 MPa, the elongation at break is 31.5%, and the shrinkage after breaking is 62%, which is the best plastic state of the material. With an acceleration in cooling, the tensile strength increases, and the elongation and shrinkage decrease, which is due to the increase in the pearlite content and results in increased obstruction to dislocation movement, increased plastic deformation resistance, and better tensile strength. When the cooling rate is 1.0 m/s, the tensile strength further increases to 895 MPa. Simultaneously, the elongation and surface shrinkage after fracture stop decreasing and begin to rise. This occurs because the uniform distribution of short-rod and GB improves the tensile strength of the steel while maintaining good plastic toughness, which corresponds to the changes in the steel structure. This high strength is well-matched with high-quality plastic toughness. It is the structure control target of high-strength steel in industrial production. With a further increase in the cooling rate, the tensile strength increases to 1019 MPa, and the plasticity of the material further deteriorates.

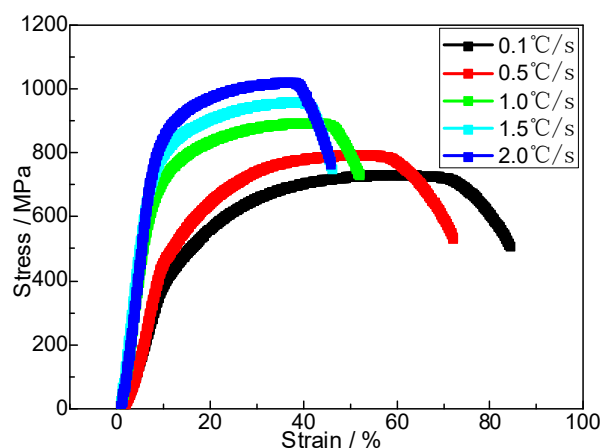


Figure 7. Tensile engineering stress–strain curves of steel at room temperature.

#### 4. Conclusions

(1) The observed microstructure of SCM435 steel cooled at different cooling rates showed that when the cooling rate was 0.1°C/s, the microstructure was an irregular polygon ferrite and lamellar pearlite; when the cooling rate was 0.5–1.0°C/s, the microstructure gradually changed to ferrite, pearlite, and GB; when the cooling rate was 1.5°C/s, the pearlite disappeared. The bainite was found to be in granular and strip form, and the first eutectoid ferrite formed. When the cooling rate reached 2°C/s, martensite precipitation appeared in the matrix.

(2) The morphology of the carbide in SCM435 steel was different under different cooling speeds. When the cooling speed was 0.1°C/s, flake carbides were distributed along the austenite in a certain orientation. When the cooling speed was 0.5°C/s, some continuous lamellar carbide grains were interrupted, and short rod-like carbides formed. When the cooling rate was above 1.5°C/s, the matrix was mainly thin-strip carbides.

(3) The grain boundary orientations in SCM435 steel were different under different cooling speeds. When the cooling speed was 0.1°C/s, the proportion of large-angle grain boundaries reached 52.8%, and the dislocation density was only  $1.91 \times 10^{12} \text{ cm}^{-2}$ ; when the cooling speed was 2.0°C/s, the proportion of large-angle grain boundaries was only 27.1%, and the dislocation density increased to  $5.38 \times 10^{12} \text{ cm}^{-2}$ .

(4) The evolution law for the surface decarburization and oxidation of SCM435 under different cooling rates. The depth of the decarburization layer showed a continuous decreasing trend with an acceleration in cooling. With the acceleration in cooling, the thickness of the oxide sheet gradually decreased. The phase structure of the oxide sheet changed such that the proportion of FeO phase gradually decreased, and the proportion of Fe<sub>3</sub>O<sub>4</sub> and Fe<sub>2</sub>O<sub>3</sub> phases gradually increased.

(5) With the increase in cooling rate, the tensile strength showed a monotonically increasing trend, whereas the elongation and shrinkage showed a fluctuating trend of first decreasing, then increasing, and then decreasing. When the cooling rate was 1.0 m/s, the short-rod and GB in the material structure endowed SCM435 steel with excellent matching strength and toughness, and its tensile strength and elongation were 895 MPa and 24%, respectively.

#### References

1. Dong H, Lian X T, Hu C D, et al. High Performance Steels: the Scenario of Theory and Technology[J]. Acta Metall. Sin., 2020, 56(4): 558
2. Hu C D, Meng L, Dong H. Research and development of ultrahigh strength steels [J]. Trans. Mater. Heat Treat., 2016, 37(11): 178
3. Hui W J, Dong H, Weng Y Q. Research and development trends of high strength steel for bolts [J]. Mater. Mech. Eng., 2002, 26(11): 1
4. Li Y B, Ma Y W, Lou M, et al. Advances in Welding and Joining Processes of Multi-material Light weight Car Body[J]. Journal of Mechanical Engineering, 2016, 52(24): 1

5. Sun H R. Review on the Fastener Steels for Automobiles[J]. *China Metall*, 2011, 21(7): 7
6. Hui W J, Zhang Y J, Zhao X L, et al. Influence of cold deformation and annealing on hydrogen embrittlement of cold hardening bainitic steel for high strength bolts[J]. *Mater. Sci. Eng.*, 2016, A 662:528
7. Wang Q, Zhu J L. Certain new techniques of wire production development in recent years[J]. *China Metall*, 2014, 24(12): 1
8. Ruan S P, Wang L J, Chen J L, et al. Effect of Control-Rolling-Cooling Process on Structure and Properties of Steel SCM435 Rod Coil[J]. *Special Steel*, 2016, 37(5):45
9. Kitadea A, Kawabataa T, Kimura S, et al. Clarification of micromechanism on Brittle Fracture Initiation Condition of TMCP Steel with MA as the trigger point[C]. *Procedia Structural Integrity* 13, 2018:1845
10. Elhigazi F, Artemev A. The influence of carbide formation in ferrite on the bainitic type transformation[J]. *Comp Mater Sci*, 2021, 186:1
11. Elhigazi F, Artemev A. The interaction between the displacive transformation and the diffusion process in the bainitic type transformation[J]. *Comp Mater Sci*, 2019, 169:1
12. Ranjan R, Singh S B. Isothermal bainite transformation in low-alloy steels: Mechanism of transformation[J]. *Acta Mater*, 2021, 202:302
13. Chen G H, Xu Y W, Liu M, et al. Effect of high-temperature deformation and undercooling on bainite transformation of a medium-carbon bainitic steel[J]. *J Iron Steel Res Int*, 2020, 32(11):984
14. Ravia A M, Kumara B A, Herbig M, et al. Impact of austenite grain boundaries and ferrite nucleation on bainite formation in steels[J]. *Acta Mater*, 2020, 188:424
15. Yong Q L, Ma M T, Wu B R. *Microalloyed Steel-Physical and Mechanical Metallurgy*[M]. Beijing: China Machine Press, 1989: 57
16. Zheng C S, Li L F, Yang W Y, et al. Microstructure evolution and mechanical properties of eutectoid steel with ultrafine or fine (ferrite+cementite) structure[J]. *Mater. Sci. Eng.*, 2014, A 599:16
17. Liang Z Y, Wang Y G, Gui Y, et al. Micro-structural evolution of oxide scales formed on a Nb-Stabilizing heat-resistant steel at the initial stage in high-temperature water vapor[J]. *Mater. Chem. Phys.* 2020, 242:1
18. Liu Y B, Zhang W, Tong Q, et al. Effects of temperature and oxygen concentration on the characteristics of decarburization of 55SiCr spring steel [J]. *ISIJ Int.*, 2014, 54: 1920
19. Noh W, Lee J M, Kim D J, et al. Effects of the residual stress, interfacial roughness and scale thickness on the spallation of oxide scale grown on hot rolled steel sheet[J]. *Mater. Sci. Eng.*, 2019, A 739:301
20. Solimani A, Nguyen T, Zhang J Q, et al. Morphology of oxide scales formed on chromium-silicon alloys at high temperatures[J]. *Corros. Sci.* 2020, 176:1
21. Huang T H, Deng C M, Song P, et al. Investigation of oxide scale formation and internal oxidation of an Fe-based coating at 500 °C and 600 °C[J]. *Surf. Coat. Technol.* 2020, 402:1

**Disclaimer/Publisher's Note:** The statements, opinions and data contained in all publications are solely those of the individual author(s) and contributor(s) and not of MDPI and/or the editor(s). MDPI and/or the editor(s) disclaim responsibility for any injury to people or property resulting from any ideas, methods, instructions or products referred to in the content.